

The physical structure of planetary nebulae around sdO stars: Abell 36, DeHt 2, and RWT 152^{*}

A. Aller^{1,2,3}, L. F. Miranda^{4,3}, L. Olguín⁵, R. Vázquez⁶, P. F. Guillén⁶, R. Oreiro⁴,
A. Ulla³, and E. Solano^{1,2}

¹*Departamento de Astrofísica, Centro de Astrobiología (INTA-CSIC), PO BOX 78, E-28691 Villanueva de la Cañada (Madrid), Spain*

²*Spanish Virtual Observatory*

³*Departamento de Física Aplicada, Universidade de Vigo, Campus Lagoas-Marcosende s/n, E-36310 Vigo, Spain*

⁴*Instituto de Astrofísica de Andalucía - CSIC, C/ Glorieta de la Astronomía s/n, E-18008 Granada, Spain*

⁵*Departamento de Investigación en Física, Universidad de Sonora, Blvd. Rosales Esq. L.D. Colosio, Edif. 3H, 83190 Hermosillo, Son. Mexico*

⁶*Instituto de Astronomía, Universidad Nacional Autónoma de México, Apdo. Postal 877, 22800 Ensenada, B.C., Mexico*

ABSTRACT

We present narrow-band $H\alpha$ and $[O\text{ III}]$ images, and high-resolution, long-slit spectra of the planetary nebulae (PNe) Abell 36, DeHt 2, and RWT 152 aimed at studying their morphology and internal kinematics. These data are complemented with intermediate-resolution, long-slit spectra to describe the spectral properties of the central stars and nebulae. The morphokinematical analysis shows that Abell 36 consists of an inner spheroid and two bright point-symmetric arcs; DeHt 2 is elliptical with protruding polar regions and a bright non-equatorial ring; and RWT 152 is bipolar. The formation of Abell 36 and DeHt 2 requires several ejection events including collimated bipolar outflows that probably are younger than and have disrupted the main shell. The nebular spectra of the three PNe show a high excitation and also suggest a possible deficiency in heavy elements in DeHt 2 and RWT 152. The spectra of the central stars strongly suggest an sdO nature and their association with PNe points out that they have most probably evolved through the asymptotic giant branch. We analyze general properties of the few known sdOs associated to PNe and find that most of them are relatively or very evolved PNe, show complex morphologies, host binary central stars, and are located at relatively high Galactic latitudes.

Key words: planetary nebulae: individual: Abell 36, DeHt 2, RWT 152 – hot subdwarfs – ISM: jet and outflows.

1 INTRODUCTION

Planetary nebulae (PNe) represent the last stage of low- and intermediate- mass stars ($0.8 \leq M/M_{\odot} \leq 8$) before ending their lives as white dwarfs. It is well known that PNe show varied morphologies that should be closely related to the mass loss history of their progenitor stars. According to Méndez (1991), most of the central stars (CSs) can be divided in two different groups: the H-rich and the H-poor CSs. However, within these two wide groups, different

classes can be found as, e.g., PG 1159, O, Wolf-Rayet-type, and hot subdwarfs CSs.

Hot subdwarf stars are evolved, low-mass ($M \approx 0.5 M_{\odot}$) stars in the extreme horizontal branch (sdBs) or beyond (sdOs). Although it is not well understood how these stars are formed, it is generally accepted that they are immediate progenitors of white dwarfs (see, e.g., Heber 2009; Geier et al 2011; Geier 2013). This would imply the possibility that many hot subdwarfs (specially the sdOs, hotter than their cousins sdBs) could be surrounded by PNe. However, there are only a few cases of confirmed sdOs as CSs and several cases of PNe whose CSs might be an sdO, although many of them lack a firm classification yet (see Aller et al. 2013 and references therein). There is scarce information about PN+sdO systems. Several works have analyzed the sdOs (or “possible” sdOs) themselves (see, e.g. Heber et al. 1988; Méndez 1991; Zijlstra 2007; Montez et al. 2010; Leone et al. 2011) but there are very few studies about their associated PNe (e.g., Méndez et al. 1988, Goldman et al. 2004). Recently, Aller et al. (2013) discovered PNG 075.9+11.6, a

^{*} Based on observations collected at the German-Spanish Astronomical Center, Calar Alto, jointly operated by the Max-Planck-Institut für Astronomie (Heidelberg) and the Instituto de Astrofísica de Andalucía (CSIC); at the Observatorio Astronómico Nacional in the Sierra San Pedro Mártir (OAN-SPM), Baja California, Mexico; and in The Isaac Newton Telescope, which is operated on the island of La Palma by the Isaac Newton Group in the Spanish Observatorio de El Roque de Los Muchachos of the Instituto de Astrofísica de Canarias.

Table 1. Common names, PNG designations, coordinates, and atmospheric parameters of the CSPNe for the objects discussed in this work.

Object	PNG	$\alpha(2000.0)$	$\delta(2000.0)$	ℓ	b	$T_{\text{eff}}[\text{K}]$	$\log g [\text{cm s}^{-2}]$
Abell 36	PNG 318.4+41.4	13 ^h 40 ^m 41 ^s .3	−19°52′55″.3	318°4	41°4	93 000 ^b – 113 000 ^c	5.3 ^b – 5.6 ^c
DeHt 2	PNG 027.6+16.9	17 ^h 41 ^m 40 ^s .9	+03°06′57″.3	027°6	16°9	117 000 ^d	5.64 ^d
RWT 152	PNG 219.2+07.5 ^a	07 ^h 29 ^m 58 ^s .5	−02°06′37″.5	219°2	07°5	45 000 ^e	4.5 ^e

^a Designation proposed in this work following the designation for Galactic PNe by Acker et al. (1992). ^bHerrero et al. (1990).

^cTraulsen et al. (2005). ^dNapiwotzki (1999). ^eEbbets & Savage (1982)

new PN around the binary sdO 2M1931+4324 (Jacoby et al. 2012). The analysis of the object revealed an extremely faint, double-shell PN, possibly deficient in heavy elements, and hinted to complex ejection processes in the formation of the nebula. Another well analysed PN+sdO system is Abell 41, a bipolar PN with a prominent equatorial ring, also around a binary sdO (Bruch et al. 2001, Shimanskii et al. 2008; Jones et al. 2010). Similar analyses of more PN+sdO systems may provide important clues about the formation and evolution of these objects.

Abell 36 and RWT 152 are two faint PNe with sdO CSs and neither their morphology nor their kinematics have previously been analyzed in detail. Abell 36 was discovered by Abell (1966) using the Palomar Observatory Sky Survey (POSS) plates and was later imaged by Hua & Kwok (1999). Its bright ($B \approx 11.3$ mag) CS was initially classified as O(H) by Acker et al. (1992) and as sdO by Kilkenny et al. (1997). Later, it was incorporated to the Subdwarf Database¹ by Østensen (2006), the most complete published compilation of hot subdwarfs to date. RWT 152 is also included in this database as an sdO, although it was previously classified as an O5 star by Chromey (1980). The PN around RWT 152 was discovered by Pritchett (1984) who found a slightly elongated nebulosity after subtracting the image of a nearby star from the image of RWT 152 itself. We have also noticed that the CS of DeHt 2 has similar spectral features to those found in sdOs (see Napiwotzki & Schönberner 1995, their Fig. 3) and, therefore, we included it in this investigation. DeHt 2 was discovered by Dengel et al. (1980) after inspecting the POSS plates. Its CS was classified as an O-type star by Acker et al. (1992) and as an hybrid-high luminosity object by Napiwotzki (1999).

In this work, we present narrow-band, optical images and high-resolution, long-slit spectroscopy of Abell 36, DeHt 2, and RWT 152, which allow us, for the first time, to describe in detail their morphology and internal kinematics. These data are complemented with intermediate-resolution, long-slit spectroscopy of the three objects to describe the nebular and CS spectra. In the case of DeHt 2, our data allow us to classify its CS as a very probable sdO. Table 1 lists a summary of the three objects: the common names and PNG designations, the equatorial and Galactic coordinates, together with the atmospheric parameters (effective temperature and surface gravity) of their CSs.

2 OBSERVATIONS

2.1 Optical imaging

Narrow-band H α , [O III], and [N II] images of Abell 36 were obtained with the Mexman filter-wheel at the 0.84 m telescope on San Pedro Mártir Observatory (OAN-SPM). The [N II] image was

taken on 2013 February 19 with a seeing of ≈ 2.8 arcsec, and the [O III] and H α images were obtained on 2013 April 7 with a seeing of ≈ 2.8 arcsec. A Marconi (e2v) CCD with 2048 \times 4612 pixels each of 15 μm in size, was used as detector in both campaigns. A 2 \times 2 binning was employed providing a field of view (fov) of $\approx 8.2 \times 18.4$ arcmin² and a plate scale of 0.468 arcsec pixel^{−1}. Total exposure time was 3600 s in the [N II] filter ($\lambda_0 = 6585$ Å, FWHM = 10 Å), 4800 s in the [O III] filter ($\lambda_0 = 5009$ Å, FWHM = 52 Å), and also 4800 s in the H α filter ($\lambda_0 = 6565$ Å, FWHM = 11 Å).

Narrow-band H α and [O III] images of DeHt 2 were obtained on 2010 August 23 with the Wide Field Camera (WFC) at the 2.5 m Isaac Newton Telescope (INT) on El Roque de Los Muchachos Observatory (La Palma, Spain). The detector of the WFC consists of four EEV 2k \times 4k CCDs with a plate scale of 0.33 arcsec pixel^{−1} and a fov of 34 \times 34 arcmin². Total exposure time was 5400 s in the [O III] filter ($\lambda_0 = 5008$ Å, FWHM = 100 Å), and 3600 s in the H α filter ($\lambda_0 = 6568$ Å, FWHM = 95 Å). We note that the H α filter includes the [N II] $\lambda\lambda 6548, 6583$ emission lines. However, these [N II] lines are not detected in the nebular spectra of DeHt 2 (see Section 3.2.3) and, therefore, the H α filter registers only the H α emission line. Seeing was ≈ 1.5 arcsec.

In the case of RWT 152, narrow-band H α and [O III] images were obtained on 2010 December 16 with the Calar Alto Faint Object Spectrograph (CAFOS) at the 2.2m telescope on Calar Alto Observatory (Almería, Spain). A SITE 2k \times 2k-CCD was used as detector, with a plate scale of 0.53 arcsec pixel^{−1} and a circular fov of 16 arcmin in diameter. Total exposure time was 900 s in [O III] filter ($\lambda_0 = 5007$ Å, FWHM = 87 Å), and 1900 s in the H α filter ($\lambda_0 = 6563$ Å, FWHM = 15 Å). Seeing was ≈ 1.5 arcsec.

The images were reduced following standard procedures within the IRAF and MIDAS packages.

2.2 Spectroscopy

2.2.1 High-resolution long-slit spectroscopy

High-resolution long-slit spectra of Abell 36, DeHt 2, and RWT 152 were obtained with the Manchester Echelle Spectrometer (MES, Meaburn et al. 2003) at the 2.1 m telescope on the OAN-SPM during two different campaigns between 2011 and 2012: Abell 36 was observed on 2012 May 12-17, DeHt 2 on 2012 May 11-13, and RWT 152 on 2011 February 17. A 2k \times 2k Marconi CCD was used as detector in 4 \times 4 binning (0.702 arcsec pixel^{−1}) in the case of Abell 36 and DeHt 2, and in 2 \times 2 binning (0.338 arcsec pixel^{−1}) in the case of RWT 152. Two filters were used: (1) a $\Delta\lambda = 60$ Å filter to isolate the H α emission line (87th order), with a dispersion of 0.11 Å pixel^{−1} (in 4 \times 4 binning) and 0.05 Å pixel^{−1} (in 2 \times 2 binning) and (2) a $\Delta\lambda = 50$ Å filter to isolate the [O III] emission line (114th order), with a dispersion 0.08 Å pixel^{−1} (in 4 \times 4 binning) and 0.04 Å pixel^{−1} (in 2 \times 2 binning). Spectra of Abell 36 and DeHt 2 were obtained with the [O III] filter and an exposure time of 1800 s

¹ <http://www.ing.iac.es/ds/sddb/>

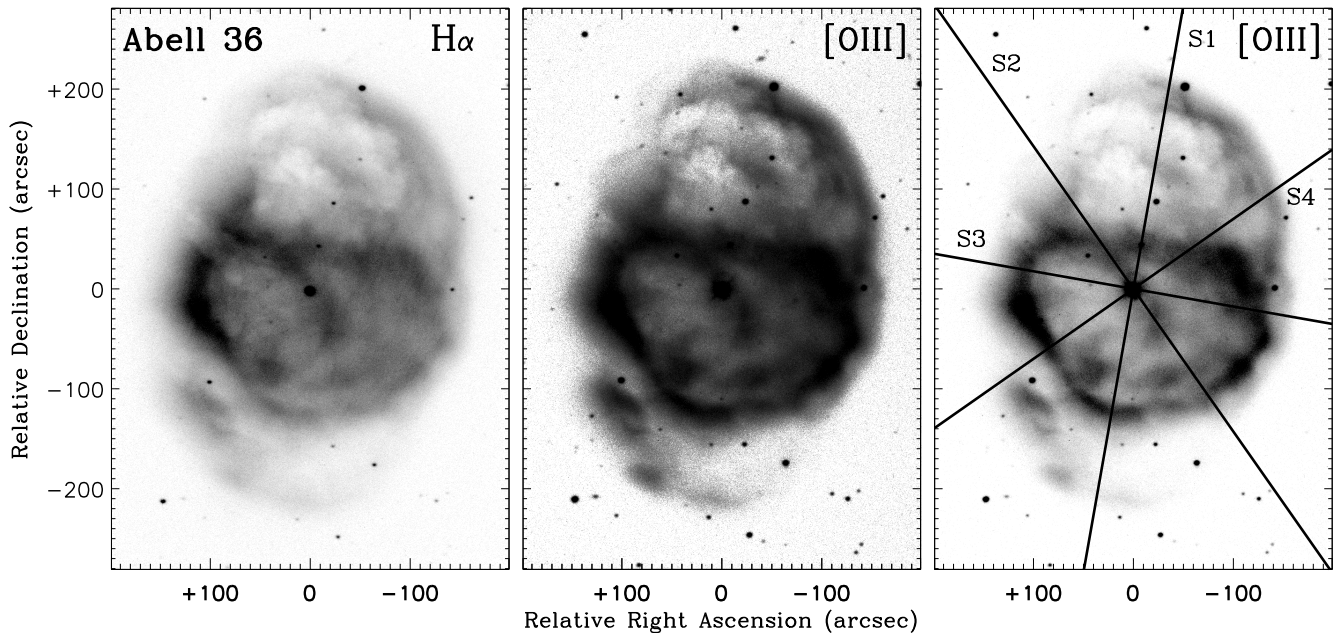


Figure 1. Grey-scale reproductions of the $H\alpha$ (left) and $[O\text{ III}]$ (middle and right) images of Abell 36. Grey levels are linear on the left and right panels and logarithmic on the middle one. Slit positions used for high-resolution, long-slit spectroscopy are drawn in the right panel (slit width not to scale).

for each individual spectrum. Spectra of RWT 152 were acquired with the $H\alpha$ and $[O\text{ III}]$ filters and exposures times of 1200 and 1800 s, respectively. For all spectra, the slit was centered on the CS of each PN and oriented at different position angles (PAs) to cover relevant morphological structures of each object. The observed PAs for each object and their choice will be described in the corresponding section dedicated to each object. The spectra were wavelength calibrated to an accuracy of $\pm 1\text{ km s}^{-1}$ using a Th-Ar lamp. The resulting spectral resolution (FWHM) is 12 km s^{-1} . Seeing was $\approx 1.5\text{--}2$ arcsec during the observations.

The spectra were reduced with standard routines for long-slit spectroscopy within the IRAF and MIDAS packages. Position-velocity (PV) maps have been obtained from these high-resolution, long-slit spectra. The origin of radial velocities in the PV maps is the systemic velocity obtained for each PN (see below), and the origin for projected angular distances is the position of the CS, as given by the intensity peak of the stellar continuum that is detected in all long-slit spectra. Internal radial velocities will be quoted hereafter with respect to the heliocentric systemic velocity of each nebula. The rest wavelengths adopted to rescale the radial velocity are 5006.84 \AA for $[O\text{ III}]$ and 6562.82 \AA for $H\alpha$.

2.2.2 Intermediate-resolution, long-slit spectroscopy

Intermediate-resolution, long-slit spectra of DeHt 2 and Abell 36 were obtained with the Boller & Chivens spectrograph mounted on the 2.1m telescope at the OAN-SPM on 2013 Jun 5 and 6, respectively. The detector was a Marconi CCD with $2k\times 2k$ pixels and a plate scale of $1.18\text{ arcsec pixel}^{-1}$. We used a 400 lines mm^{-1} dispersion grating, giving a dispersion of $1.7\text{ \AA pixel}^{-1}$, and covering the $4100\text{--}7600\text{ \AA}$ spectral range. In the case of DeHt 2 a spectrum with the slit at $PA\ 55^\circ$ was obtained with the slit centered on the CS. In the case of Abell 36 a spectrum with the slit at $PA\ 90^\circ$ was obtained covering the CS and the eastern part of the nebula. For both objects,

the slit width was 2 arcsec and exposure time was 1800 s for each spectrum. Seeing was ≈ 3 arcsec.

Intermediate-resolution, long-slit spectra of RWT 152 were obtained using CAFOS at the 2.2m telescope on Calar Alto Observatory on 2010 December 17. The detector was a SITE $2k\times 2k$ -CCD with a plate scale of $0.53\text{ arcsec pixel}^{-1}$. Gratings B-100 and R-100 were used to cover the $3200\text{--}6200\text{ \AA}$ and $5800\text{--}9600\text{ \AA}$ spectral ranges, respectively, both at a dispersion of $\approx 2\text{ \AA pixel}^{-1}$. The spectra were taken with the slit at $PA\ 0^\circ$ and exposure times was 900 s for each grism. The slit width was 2 arcsec and it was centered on the CS. Seeing was ≈ 2 arcsec. Spectrophotometric standards stars were observed each night for flux calibration.

The spectra were reduced using standard procedures for long-slit spectroscopy within the IRAF and MIDAS packages. For each PN, the observed emission line fluxes were dereddened using the extinction law of Seaton (1979) and the corresponding logarithmic extinction coefficient $c(H\beta)$, as obtained from the $H\alpha/H\beta$ observed flux ratio, assuming Case B recombination ($T_e=10^4\text{ K}$, $N_e=10^4\text{ cm}^{-3}$) and a theoretical $H\alpha/H\beta$ ratio of 2.85 (Brocklehurst 1971).

3 RESULTS

3.1 Abell 36

3.1.1 Imaging

Figure 1 shows our $H\alpha$ and $[O\text{ III}]$ images of Abell 36. Our $[N\text{ II}]$ image does not show nebular emission and is not presented here. Abell 36 presents an elliptical morphology with the major axis oriented at $PA\ \approx 350^\circ$, and a size of $\approx 7.4\times 5.3\text{ arcmin}^2$. Two particularly bright point-symmetric knotty arcs are observed, giving a spiral appearance to Abell 36, as already noted by Hua & Kwok (1999). Our images also suggest that a faint elliptical envelope could encircle the rest of components. The nebular emission is

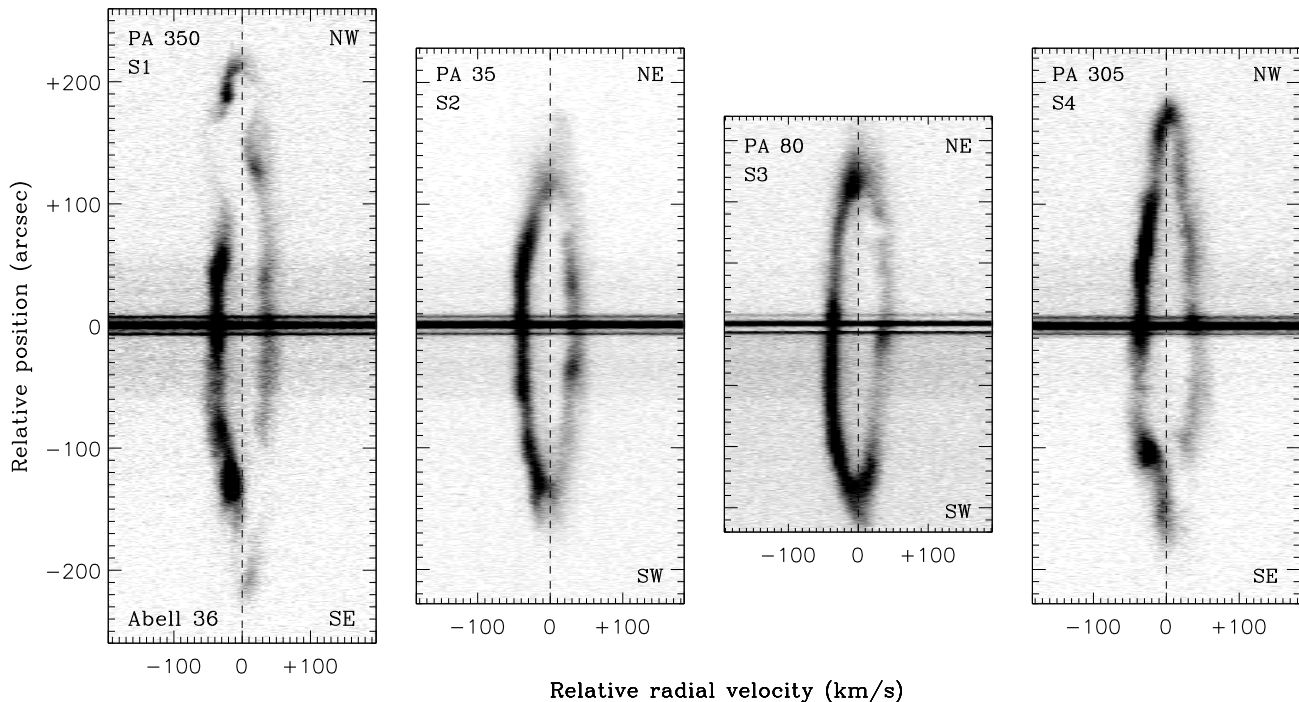


Figure 2. Grey-scale, PV maps derived from the high-resolution, long-slit [O III] spectra of Abell 36 at four different PAs (upper left corner in each panel, see also Fig. 1). Grey levels are linear. The origin is at the systemic velocity (see text) and position of the CS, as indicated by the stellar continuum. The two horizontal emission features parallel to the continuum of the CS is a well characterized reflection of the instrument.

dominated, particularly in [O III], by a distorted ring-like structure of $\approx 3.3 \times 5.3 \text{ arcmin}^2$ in size, that appears displaced towards the south with respect to the CS. Several bright knots are also observed inside this ring. Towards the north, a bubble-like structure can be recognized inside the elliptical shell, that apparently emanates from the ring. The bubble extends up to $\approx 2.6 \text{ arcmin}$ from the CS and is oriented at $\text{PA} \approx 12^\circ$ that is different from the orientation of the major axis of the ellipse.

3.1.2 High-resolution, long-slit spectroscopy

Spectra of Abell 36 were obtained at PAs 35° , 80° , 305° , and 350° . The slit positions are shown in Fig. 1 (right panel) overimposed on the [O III] image of the nebula, and are denoted from S1 to S4 starting at PA 350° counterclockwise. The slit PAs were chosen to cover the major and minor axis (S1 and S3, respectively) of the ellipse as well as two intermediate PAs (S2 and S4). It should be noted that in the cases of PAs 35° , 305° , and 350° , two spectra were secured with the slit on the CS but displaced from each other along the corresponding PA to cover the whole nebula. These two spectra were combined during the reduction process into a single long-slit spectrum. Figure 2 shows the PV maps of the [O III] emission line at the four observed PAs. From the radial velocity centroid of the [O III] emission feature we derive a heliocentric systemic velocity $V_{\text{HEL}} = +34.8 \pm 1.4 \text{ km s}^{-1}$, in agreement with the value obtained by Bohuski & Smith (1974).

The PV maps show a velocity ellipse with maximum velocity splitting of $\approx 74 \text{ km s}^{-1}$ at the stellar position and with no particular tilt with respect to the angular axis. The spatio-kinematical properties of the velocity ellipse vary with PA. In addition, outer

structures are also distinguished. We describe below the PV maps in more detail.

The velocity ellipses at PAs 35° and 80° (S2 and S3 in Figs. 1 and 2) present similar properties to each other. They extend up to $\approx 130 \text{ arcsec}$ towards the NE and $\approx 105 \text{ arcsec}$ towards the SW. The size of the velocity ellipses fits very well the size of the bubble and the southern part of the distorted ring (see Fig. 1), suggesting a spatio-kinematical relationship between both structures.

The PV map at 350° (S1 in Fig. 1) reveals a more complex kinematics. The velocity ellipse extends between $\approx \pm 130 \text{ arcsec}$ from the CS. Two bright knots are observed close to its tips with radial velocities of $\approx \pm 20 \text{ km s}^{-1}$ (NW knot redshifted). A comparison with the images in Fig. 1 shows that these knots correspond to cuts of slit S1 with the bright edge of the northern bubble and with the southern edge of the distorted ring. This result reinforces those obtained at PAs 35° and 80° that the northern bubble and the southern half of the observed ring form a unique spatio-kinematic structure that may be defined as a spheroid. It is noteworthy that this spheroid has been identified through an analysis of PV maps based on high-resolution spectra and that it can be hardly recognized in the direct images. In addition, these spectra also demonstrate that the distorted ring observed in the direct images is a projection effect and does not correspond to a real nebular structure. We also note that the velocity ellipse appears to be open at two point-symmetric locations on the PV map, with the NW “hole” mainly blueshifted and the SE one mainly redshifted. Moreover, towards the NW, faint emission, with an arcuate shape in the PV map, and radial velocities up to $\approx -55 \text{ km s}^{-1}$, connects the velocity ellipse with emission from the NW point-symmetric arc. The NW arc itself presents two radial velocity components centered at the systemic velocity, with

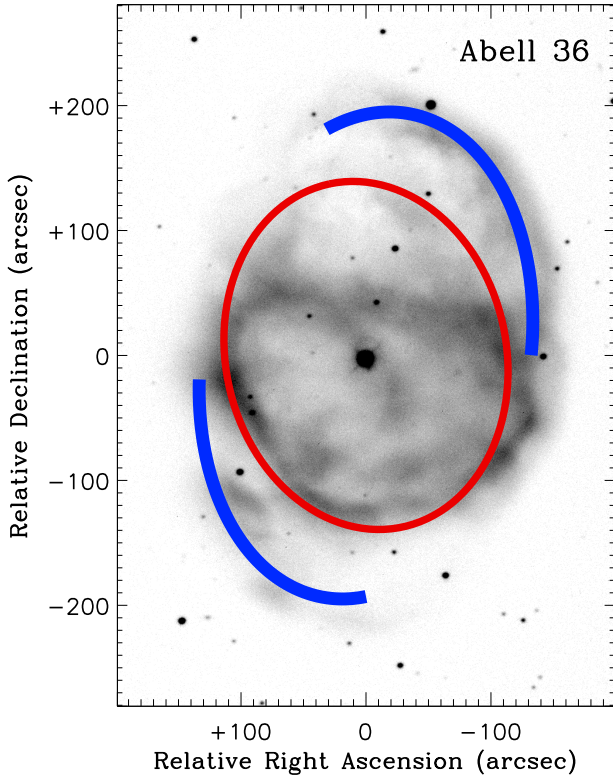


Figure 3. Sketch of Abell 36 as derived from our morphokinematical analysis. The spheroidal shell is displayed in red and the bright arcs are represented by thick blue lines (see the electronic edition for a color version of this figure).

the brightest component being slightly blueshifted. The emission feature due to the SE arcs is similar to that of the NW arcs, but fainter and slightly redshifted.

At PA 305° (S4 in Fig. 1) the velocity ellipse may also be recognized, although it appears open at its tips and connected to emission from the point-symmetric arcs. This velocity ellipse is also compatible with the spheroidal structures identified at the other PAs. Emission from the NW arc present two velocity components, although it is centered close to the systemic velocity. Emission from the SE arc shows a single velocity component at the systemic velocity.

Some of the bright knots observed in the inner nebular regions have been covered by the slits (see Fig. 1). These knots do not appear as separated entities in the PV maps but share the kinematics of the velocity ellipses, suggesting that they are a part of the spheroidal structure.

The PV maps (Fig. 2) reveal that the [O III] emission is noticeable stronger in the blueshifted part of the nebula than in the redshifted one, as observed in other PNe (e.g., IC 2149, Vázquez et al 2002). This could be related to dust absorption of the redshifted emission. Alternatively, interaction of the front (blueshifted) half of Abell 36 with the ISM could be causing this effect. To test this possibility, we compare the radial velocity of the local ISM at the position of Abell 36 with that of the nebula itself, assuming a distance of 150–770 pc (see Abell 1966; Cahn & Kaler 1971; Cahn, Kaler & Stanghellini 1992; Acker 1998; Phillips 2005) and a stan-

Table 2. Emission line intensities in Abell 36.

Line	$f(\lambda)$	$I(\lambda) I(\text{H}\beta)=100$
H γ λ 4340	0.129	46.5 \pm 0.7
He II λ 4686	0.042	123.0 \pm 1.0
He I+[Ar IV] λ 4711	0.036	16.7 \pm 0.3
[Ar IV] λ 4740	0.029	8.4 \pm 0.4
H β λ 4861	0.000	100.0 \pm 1.0
[O III] λ 4959	-0.023	96.9 \pm 1.0
[O III] λ 5007	-0.034	278.6 \pm 2.2
He II λ 5411	-0.118	9.5 \pm 0.3
H α λ 6563	-0.323	285.0 \pm 1.4
$c(\text{H}\beta) = 0.17$		
$\log F_{\text{H}\beta}(\text{erg cm}^{-2} \text{s}^{-1}) = -13.34$		

dard rotation curve of the Galaxy. Following the formulation by Nakanishi & Sofue (2003), we obtain a heliocentric radial velocity of $\approx +26 \text{ km s}^{-1}$ for the ISM around Abell 36, that is lower than that of the nebula ($\approx +35 \text{ km s}^{-1}$). These values suggest that Abell 36 is encroaching on the ISM, although one would expect that the rear (redshifted) half of Abell 36 was the brighter one, while the opposite is observed.

The analysis of the PV maps implies a physical structure for Abell 36 that is quite different from what could be expected from the images. Figure 3 shows a sketch of the nebula overlaid on the [O III] image. As already mentioned, the velocity ellipse observed at all PAs is compatible with a spheroidal structure. Its major axis should be almost perpendicular to the line of sight, as indicated by the lack of tilt of the velocity ellipse in the PV maps, and oriented at PA around 12°, as suggested by the orientation of the northern bubble. The arcs resemble the point-symmetric structures observed in other PNe (e.g., NGC 6309, Vázquez et al. 2008). Hua & Kwok (1999) compared Abell 36 with NGC 6543 and our results strength this comparison and extend it to IC 4364 as well. These three PNe show a spheroidal/ellipsoidal shell that is accompanied by outer and extended point-symmetric regions (components DD' in NGC 6543 [Miranda & Solf 1992] and in IC 4364 [Guerero et al. 2008] and point-symmetric arcs in Abell 36), which appear twisted with respect to the orientation of the spheroidal shell. Following these authors, the point-symmetric arcs of Abell 36 may be interpreted as due to a collimated bipolar outflow that has been ejected along a rotating axis. If so, the axis has rotated mainly in a plane (the plane of the sky) as indicated by the low radial velocity of the arcs, while a relatively large rotation angle of $\approx 100^\circ$ is inferred from the images.

The velocity ellipses appear disrupted at PAs 305° and 350°, where the bright arcs are observed, but not at PAs 35° and 80°, where the bright arcs do not extend. This strongly suggests a relationship between the bright arcs and the disrupted regions of the spheroid. In particular, this disruption could be originated by a collimated outflow that is able to go through the spheroid, perforating parts of it. The kinematics of the faint emission connecting the velocity ellipse and the emission features from the arcs observed in the PV map at PA 305° strongly suggests an acceleration of material from the spheroid followed by a more or less sudden deceleration that could be due to interaction with the faint elliptical envelope. It is worth noting that, if this interpretation is correct, the collimation degree of the bipolar outflow should have been very high because only “relatively” small portions of the spheroid are disrupted

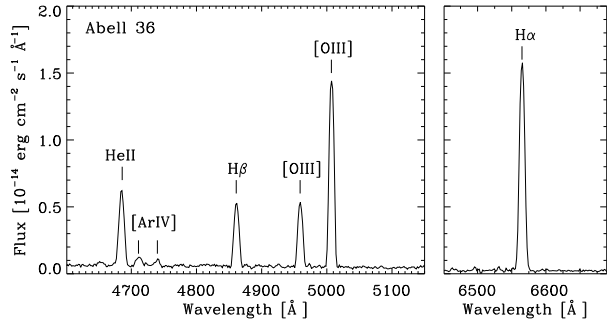


Figure 4. Nebular spectrum of Abell 36 obtained by integrating the emission lines between 77 and 124 arcsec eastern from the CS along the slit position. The emission lines are labelled.

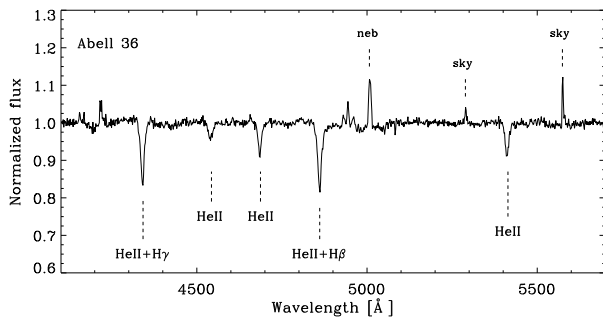


Figure 5. Normalized optical spectrum of the CS of Abell 36. Poorly subtracted sky lines and nebular emission lines are marked as well as some absorption lines.

at each PA and a velocity ellipse can still be recognized in the PV maps at PAs 305° and 350°.

The equatorial expansion velocity of the spheroid ($\sim 37 \text{ km s}^{-1}$), its equatorial radius ($\sim 1.7 \text{ arcmin}$), and the distance (150–770 pc, see above) yield a kinematical age of $\sim 2\text{--}10 \times 10^3 \text{ yr}$, a broad range of ages given by the uncertainty in the distance, that is compatible with a relatively young or very evolved PN. Finally, if our interpretation of the bright arcs is correct, the corresponding collimated outflows should be younger than the spheroid. However, their kinematical age is impossible to obtain because their original velocity is unknown as well as the changes their velocity may have suffered through collimated outflow–shell interaction.

3.1.3 Intermediate-resolution, long-slit spectroscopy

The intermediate-resolution, long-slit nebular spectrum of Abell 36 is presented in Figure 4. A logarithmic extinction coefficient $c(\text{H}\beta)$ of ≈ 0.17 was obtained (see § 2.2.2). The dereddened line intensities and their Poissonian errors are listed in Table 2. In addition to the hydrogen and [O III] $\lambda\lambda 4959, 5007$ emission lines, strong high excitation emission lines are observed as He II $\lambda 4686$ and [Ar IV] $\lambda\lambda 4711, 4740$. We note that [O III] $\lambda 4363$ and [Ar V] $\lambda 7005$ line emissions could also be present but deeper spectra are needed to confirm them. The spectrum indicates a high-excitation nebula, which is compatible with the non detection of the nebula in the [N II] filter.

The normalized spectrum of the CS of Abell 36 is shown in Figure 5. As already mentioned, this star is included in the Subdwarf Database by Østensen (2006). The presence of narrow He II

absorption lines (specially He II $\lambda 4686$) as well as the atmospheric parameters (Table 1) are indeed compatible with an sdO nature.

3.2 DeHt 2

3.2.1 Imaging

Figure 6 shows our H α and [O III] images of DeHt 2 that reveal more details than previous ones (Manchado et al. 1996). They show an elliptical shell with a size of $\approx 1.9 \times 1.5 \text{ arcmin}^2$ and major axis oriented at PA $\approx 55^\circ$, although the polar regions seem to protrude and deviate from a “pure” elliptical geometry, in particular at the SW region. The shell shows a limb-brightening that is more noticeable along the northern edge. This could be a result of interaction of the nebula with the interstellar medium (Wareing et al. 2007), an idea that is supported by the fact that the limb-brightening is more noticeable in [O III] than in H α . Two bright filaments are observed in [O III] (much weaker in H α) at the NE tip of the shell. They are parallel to each other, separated $\approx 0.1 \text{ arcmin}$, and oriented perpendicular to the major nebular axis. Furthermore, the images reveals the existence of an (elliptical) ring embedded in the elliptical shell, that is mainly distinguished by its relative brightness. The size of the ring is $\approx 1.5 \times 0.7 \text{ arcmin}^2$ and its minor axis is oriented E-W approximately. This ring is drawn in Fig. 6. The orientations of the ring and the elliptical shell are quite different from each other, indicating that the ring does not trace the equatorial plane of the elliptical shell.

3.2.2 High-resolution, long-slit spectroscopy

Spectra of DeHt 2 were obtained at PAs 0°, 50°, 90°, and 140°. These slit positions (denoted S1 to S4, respectively) are plotted in Fig. 6 (right panel), on the [O III] image of the nebula. Slits S1 and S3 were chosen to cover the major and minor axes of the ring, respectively, while S2 covers the main axis of the elliptical shell and S4 its minor axis. Figure 7 shows the PV maps of the [O III] emission line at the four observed PAs. From the radial velocity centroid of the line emission feature we derive a heliocentric systemic velocity $V_{\text{HEL}} = +47 \pm 2 \text{ km s}^{-1}$.

The PV maps at PAs 0° and 140° mainly show a velocity ellipse. The ellipse does not appear tilted on these PV maps, although some asymmetries with respect to the velocity axis are observed. At PA 50° the emission line feature shows a spindle-like shape slightly tilted in the PV map such the NE (SW) regions present an excess of blueshifted (redshifted) radial velocities. At PA 90° the emission line feature shows a shape halfway between that observed at PA 50° and PA 140°. Maximum line splitting of $\approx 100 \text{ km s}^{-1}$ is observed at the stellar position at all PAs. The PV maps also show that the CS is displaced from the nebular centre $\approx 3 \text{ arcsec}$ towards the southwest at PA 50° and $\approx 5 \text{ arcsec}$ towards the west at PA 90°, which is difficult to recognize in the direct images. By combining these shifts, the CS appears displaced $\approx 7.5 \text{ arcsec}$ towards PA $\approx 255^\circ$.

The [O III] emission feature is generally weak in the PV maps except at particular positions that correspond to well identified regions in the images. The two bright filaments at the NE tip of the elliptical shell can be recognized on the PV map at PA 50°, as two knots with radial velocities of $\approx -18 \text{ km s}^{-1}$ at $\approx 0.9 \text{ arcmin}$ from the CS and -10 km s^{-1} at $\approx 1 \text{ arcmin}$. The SW tip of the elliptical shell also appears bright in the PV map with a radial velocity of $\approx +16 \text{ km s}^{-1}$ at $\approx 0.9 \text{ arcmin}$. The rest of bright regions on PV maps coincide with the ring identified in the images. Although these features appear elongated in the spatial direction (particularly at PA

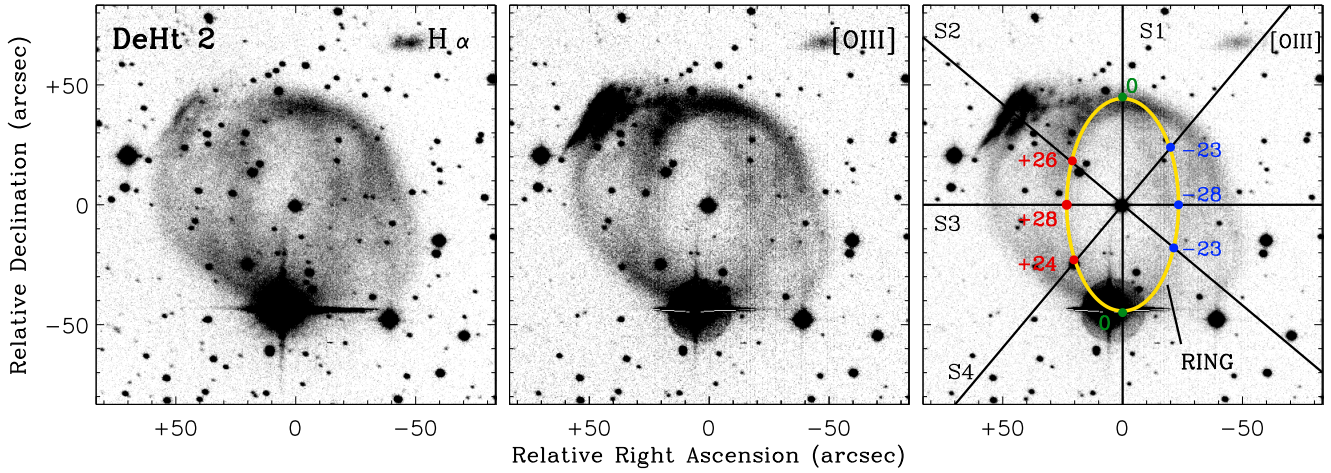


Figure 6. Grey-scale reproductions of the $H\alpha$ (left) and $[O\text{III}]$ (middle and right) images of DeHt 2. Grey levels are linear. Slit positions used for the high-resolution, long-slit spectroscopy are drawn on the right panel (slit width not to scale). The small nebulosity towards the northwestern of DeHt 2 could be a galaxy (see the electronic edition for a color version of this figure).

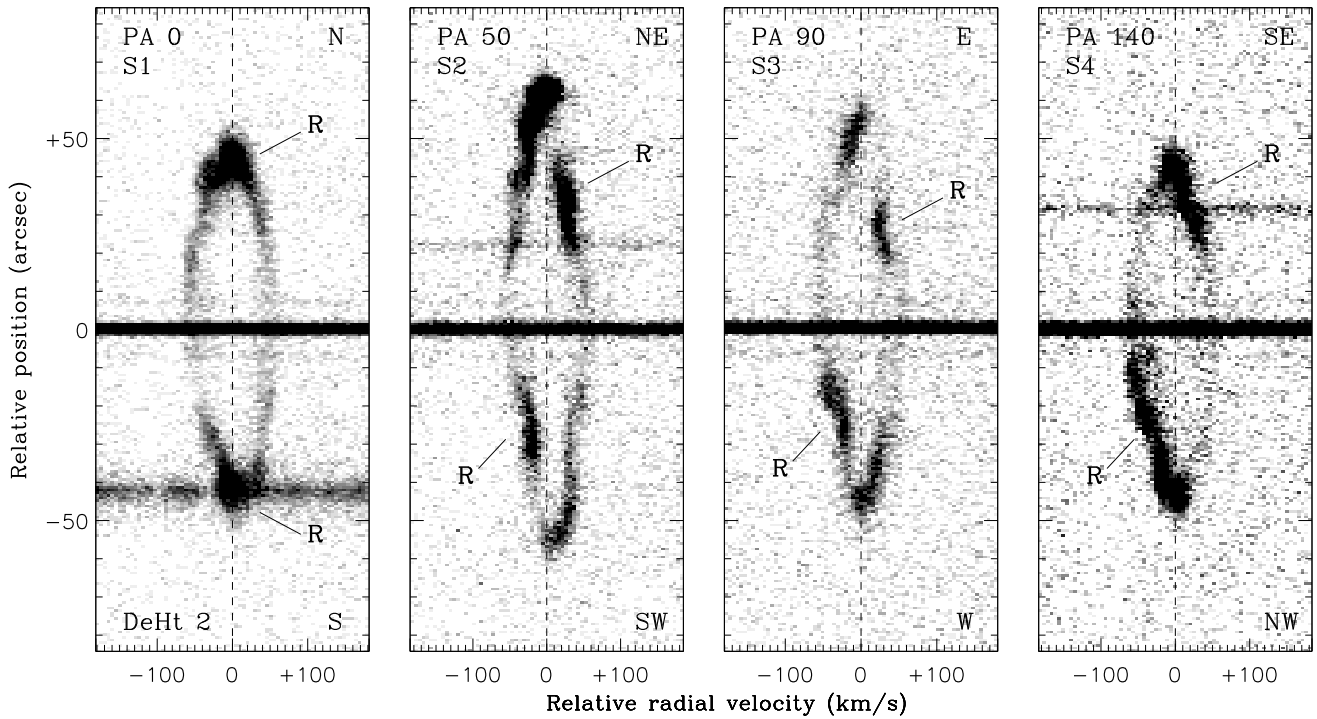


Figure 7. Grey-scale, PV maps derived from the high-resolution, long-slit $[O\text{III}]$ spectra of DeHt 2 at four different PAs (upper left, see also Fig. 6). The bright features related to the ring-like structure are indicated by ‘R’.

140°) and the radial velocity is difficult to measure, we have considered the position observed in the direct images to obtain the radial velocity that is indicated in Fig 6 (right panel). The western half of the ring is blueshifted while the eastern half is redshifted. Moreover, the radial velocity presents systematic variations in the ring reaching a maximum (in absolute value) of $\approx 28 \text{ km s}^{-1}$ at the minor axis, a minimum value of $\approx 0 \text{ km s}^{-1}$ at the major axis, and intermediate values at PAs 50° and 140°. This kinematics coincides

with that expected from a tilted circular ring. Under this assumption, we obtain an inclination angle of $\approx 30^\circ$ for the plane of the ring with respect to the line of sight, an expansion velocity of $\approx 36 \text{ km s}^{-1}$, and a PA of $\approx 96^\circ$ for the orientation of the ring axis. It is noteworthy that the expansion velocity of the ring is lower than the expansion velocity measured at the stellar position, $\approx 50 \text{ km s}^{-1}$, as indicated by the maximum radial velocity splitting of the velocity ellipse.

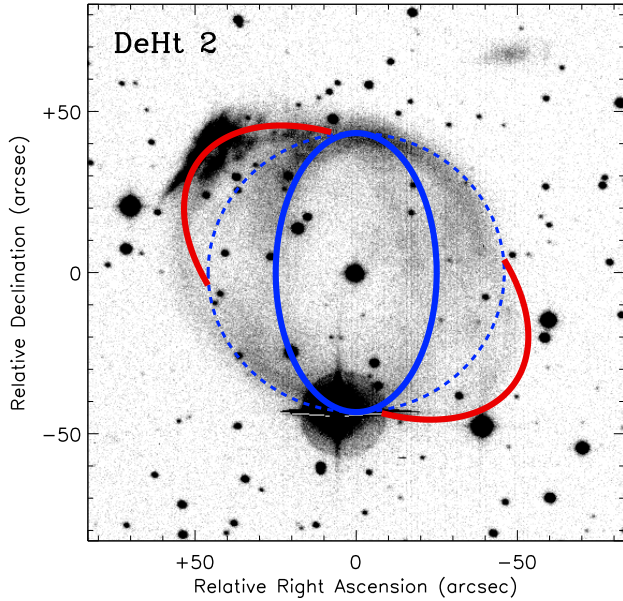


Figure 8. Sketch of the DeHt 2, as derived from our morphokinematical analysis. The spheroidal shell (dashed blue line), the ring-like structure (solid blue line), and the bipolar outflow (solid red line) are drawn (see the electronic edition for a color version of this figure).

The spatio-kinematical properties of DeHt 2 indicate that its formation has been complex with at least two different ejection processes being involved. In Figure 8 we show a schematic representation of the structures that compose DeHt 2, as inferred from the analysis of the PV maps. We suggest that the original structure of this PN was a spheroid on which a bright, ring-like region defined its equatorial plane. The fact that the expansion velocity of the ring (36 km s^{-1}) is lower than that measured at the stellar position (50 km s^{-1}) (at some latitude above the equator), strongly suggests that the original structure was not spherical but probably an ellipsoid with the major axis oriented approximately E-W. Taken into account the spatio-kinematical properties of the ring and assuming a distance of 1.9–3.2 kpc (Dengel 1980; Napiwotzki 1999, 2001), its kinematical age results to be $1.3\text{--}1.9 \times 10^4$ yr, compatible with an evolved PN. Probably later, another bipolar ejection has taken place, that interacted with and deformed the original spheroid, as suggested by the protruding regions that are now observed as the polar regions of the apparent elliptical shell. The second ejection should have been collimated and along a bipolar axis oriented at $\text{PA} \approx 50^\circ$ that is different from the orientation of the previous structure.

3.2.3 Intermediate-resolution, long-slit spectroscopy

Figure 9 shows the intermediate-resolution, long-slit spectra of the NE filaments of DeHt 2. Only the $\text{H}\alpha$, $\text{H}\beta$, $[\text{OIII}]\lambda 4959, 5007$, and $\text{HeII}\lambda 4686$ emission lines are detected. A logarithmic extinction coefficient $c(\text{H}\beta) \approx 0.33$ was obtained (see § 2.2.2). The dereddened line intensities and their Poissonian errors are listed in Table 3. The spectrum indicates a very high excitation although other high-excitation emission lines (as in the case of Abell 36) are not observed. The same emission lines are detected in other nebular regions (spectra not shown here), suggesting a somewhat lower excitation than in the NE filaments.

Table 3. Emission line intensities in DeHt 2.

Line	$f(\lambda)$	$I(\lambda) I(\text{H}\beta)=100$
He II $\lambda 4686$	0.042	103.7 ± 2.7
H β $\lambda 4861$	0.000	100.0 ± 2.8
[O III] $\lambda 4959$	-0.023	308.5 ± 3.6
[O III] $\lambda 5007$	-0.034	921.1 ± 6.5
H α $\lambda 6563$	-0.323	285.0 ± 4.3

$c(\text{H}\beta) = 0.33$
 $\log F_{\text{H}\beta} (\text{erg cm}^{-2} \text{ s}^{-1}) = -14.63$

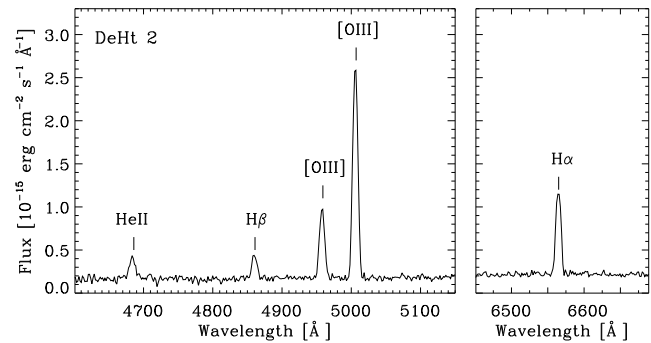


Figure 9. Nebular spectrum of DeHt 2 obtained by integrating the long-slit spectrum between 0.8 and 1.1 arcmin from the CS along $\text{PA} = 55^\circ$. The spectrum corresponds to the bright filaments at the northeastern (see Fig. 6).

The stellar spectrum is shown in Figure 10. It shows strong He II absorptions some of which can be blended with the Balmer absorptions. Although the spectrum of DeHt 2 does not have enough spectral resolution to resolve the Pickering and Balmer absorption lines, most probably the absorptions present in this spectrum mainly correspond to the Pickering ones, due to the high effective temperature of this CS (117000 K, see Table 1). These spectral features and the atmospheric parameters (Table 1) are compatible with a very hot sdO star. To provide more support for this classification, we compare in Figure 10 the normalized blue spectrum of the CS with that of BD+28°4211, a well known sdO with $T_{\text{eff}} \approx 82000$ K and $\log g \approx 6.2 \text{ cm s}^{-2}$ (Latour et al. 2013). The spectrum of BD+28°4211 was obtained with the CAFOS spectrograph on 2011 July. Spectra of both stars are also shown in Napiwotzki & Schonberner (1995, their Fig. 3). Both spectra are remarkably similar to each other, being the observed differences probably due to the signal to noise in each spectra and to the different atmospheric parameters of the stars. In any case, the spectral similarities strongly suggest an sdO nature for the CS of DeHt 2.

3.3 RWT 152

3.3.1 Imaging

Figure 11 shows the $\text{H}\alpha$ and $[\text{O III}]$ images of RWT 152, in which details of the nebular morphology can be distinguished for the first time. Both images reveal a very faint PN. While in the $\text{H}\alpha$ image the nebula presents a diffuse, although non spherical appearance, a more defined nebula can be discerned in the $[\text{O III}]$ image. At low intensity levels, the nebula seems to be almost circular whereas at higher intensity levels, it appears slightly bipolar with a size of $\approx 17 \times 21 \text{ arcsec}^2$, major axis oriented at $\text{PA} \approx 40^\circ$, and a rather uni-

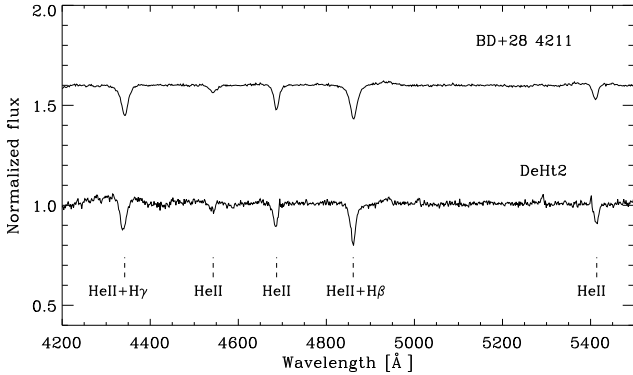


Figure 10. Normalized optical spectrum of the CS of DeHt 2 (bottom) compared to that of BD+28°4211 (top).

form intensity distribution. It is worth noting that the CS is clearly displaced towards the northwest with respect to the center of the nebula (see also below).

3.3.2 High-resolution, long-slit spectroscopy

Spectra of RWT 152 were obtained at PA 45° (in H α and [O III]) and PA 135° (in [O III]) to cover the major and minor axis (S1 and S2, respectively, in Fig. 11) of the bipolar shell. Figure 12 shows the two PV maps in the [O III] emission line. We note that the [O III] emission line feature presents a much more knotty appearance in the PV maps than in the image. The PV map of H α emission line at PA 45° (not shown here) is very similar to that of the [O III] emission line at the same PA, but the large thermal width in the H α line does not allow us a detailed analysis of the kinematics. From the velocity centroid of the line emission features we derive a heliocentric systemic velocity of $V_{\text{HEL}} = +134.5 \pm 1.8 \text{ km s}^{-1}$.

In the PV map at PA 45°, the [O III] emission feature presents an hour-glass like shape with a size of ≈ 22 arcsec, although deviations from a pure hour-glass shape are noticed, particularly in the NE lobe. Radial velocity at the tips of the emission feature is $\approx \pm 7 \text{ km s}^{-1}$. Two bright knots can be distinguished in the central region, that are symmetric in radial velocity but not centered on the CS: the redshifted knot presents a radial velocity of $\approx +14 \text{ km s}^{-1}$ and is located ≈ 0.12 arcsec NE from the CS; the blueshifted one has a radial velocity of $\approx -14 \text{ km s}^{-1}$ and is located ≈ 1.8 arcsec SW from the CS. The PV map at PA 135° presents a velocity ellipse with a maximum line splitting of $\approx 34 \text{ km s}^{-1}$ at the stellar position and a size of ≈ 18 arcsec as measured between the intensity peaks at the systemic velocity. The centre of the velocity ellipse is displaced ≈ 1.2 arcsec towards the SE with respect to the CS.

The displacements of nebula’s centre with respect to the CS as measured in the PV maps are consistent with the off-centre position of the CS observed in the direct images. Taken into account the two observed PAs, a shift of ≈ 1.4 arcsec towards PA $\approx 348^\circ$ is obtained.

Both images and PV maps are compatible with a bipolar PN. The two bright knots observed in the central regions in the PV map at PA 45° suggest the existence of an equatorial enhancement. If we assume circular cross section for the equator, the equatorial plane of the nebula is tilted by $\approx 6^\circ$ with respect to the line of sight. Assuming homologous expansion, a polar velocity of 19 km s^{-1} is obtained. There is no reliable determination for the distance of RWT 152 and estimates are 1.4 and 6.5 kpc (Ebbets & Savage 1982;

Pritchett 1984). In consequence, only a lower limit of $\approx 4 \times 10^3$ yr can be obtained for its kinematical age, which suggests (at least) a relatively evolved PN.

3.3.3 Intermediate-resolution, long-slit spectroscopy

The intermediate-resolution nebular spectrum of RWT 152 is presented in Figure 13. Only the H α , H β and [O III] $\lambda\lambda 4959, 5007$ emission lines are identified. A logarithmic extinction coefficient $c(\text{H}\beta)$ of ≈ 0.46 was derived (see § 2.2.2). Table 4 lists the dereddened line intensities and their Poissonian errors. The [O III]/H β line intensity ratio is ≈ 8 (Table 4), suggesting a relatively high excitation.

The normalized spectrum of the CS is shown in Figure 14. In contrast to the CS spectrum of DeHt 2, the CS spectrum of RWT 152 is dominated by hydrogen Balmer lines. The narrowness of the absorption lines, and the presence of He I (e.g. He I $\lambda\lambda 4386, 4471$) and He II absorption lines (specially He II $\lambda 4686$) confirm the sdO nature of the CS. The CS was analyzed by Ebbets & Savage (1982) who determined a relatively low (for an sdO) T_{eff} of $\approx 45000 \text{ K}$ (see Table 1) that is compatible with the presence of He I $\lambda 4471$.

4 DISCUSSION

The data presented and analyzed in the previous sections have allowed us to deduce the basic physical structure and emission properties of Abell 36, DeHt 2, and RWT 152 and their CSs. Moreover, the spatio-kinematical analysis has been able to recover relevant information about the processes involved in the formation of the three objects. In addition, the spectra of the three CSs show characteristics that allow us to classify them as sdOs. In particular, the narrowness of the absorption lines and the presence of prominent He II absorption are typical of sdOs. This classification is corroborated by the atmospheric parameters of the CSs (Table 1), that are within the range of the sdOs atmospheric parameters (see Heber 2009).

RWT 152 seems to be a result of a typical bipolar ejection as observed in many PNe. The formation of Abell 36 and DeHt 2 appears more complex and requires multiple ejection events, changes in the orientation of main ejection axis between events, and a different collimation degree of the ejections. In Abell 36 the bright arcs indicate a very large and “continuous” change in the collimated ejection axis, whereas in DeHt 2 the bipolar outflows seem to have acted along a constant direction that is different from the main axis of the previous shell. Interestingly, evidence is found in both PNe that the collimated outflows might have been ejected after the main nebular shell was formed. Moreover, in both cases, the collimated outflows seem to have disrupted or deformed the previous shell. This situation is similar to that found in other PNe (e.g., Guerrero & Miranda 2012; Ramos-Larios et al. 2012; Guillén et al. 2013) in which young collimated outflows seem to have disrupted a previous nebular structures. The origin of collimated outflows in PNe after the formation of the main nebular shell is difficult to explain within current scenarios for PN formation and is still matter of debate (see Tocknell, De Marco & Wardle 2014).

Multiple ejection events, as those identified in Abell 36 and DeHt 2, are observed in many PNe. The idea that complex PNe are related to the evolution of binary CSs has been present during many years and it has received strong support with recent detections of new binary CSs in PNe with multiple structures and jets (see Miszalski et al. 2009 and references therein). Within this context, it

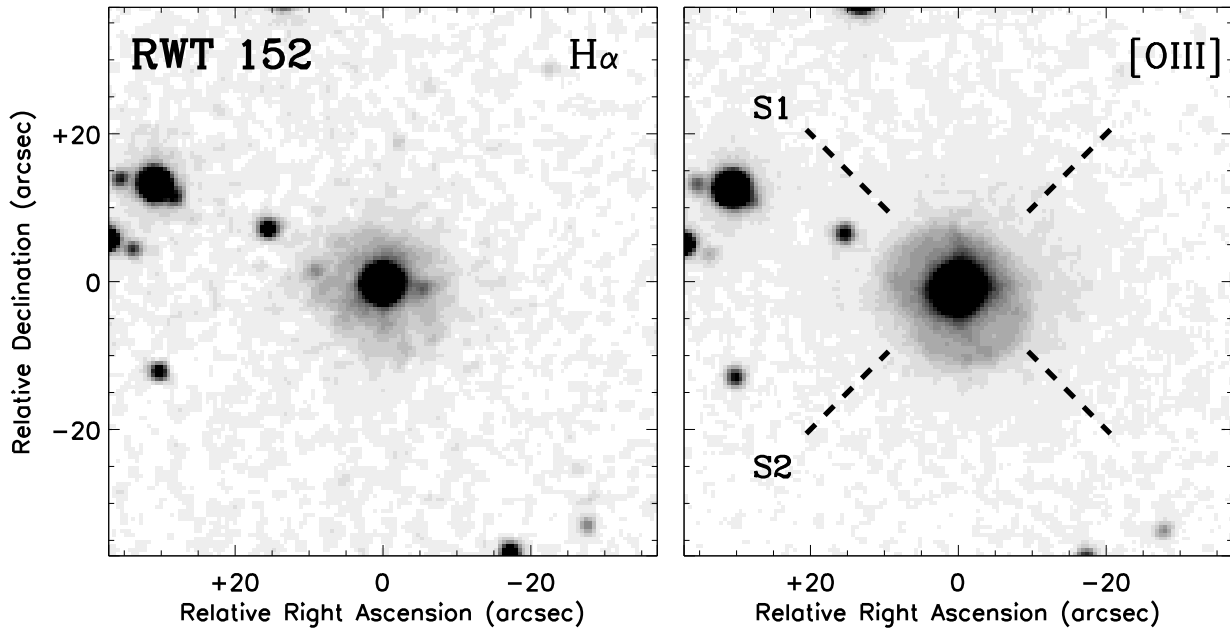


Figure 11. Grey-scale reproductions of the $H\alpha$ and $[O\text{III}]$ images of RWT 152. Grey-levels are linear. A 3×3 box smooth was used for the representation. The slit positions used for the high-resolution, long-slit spectroscopy (S1 and S2) are drawn in the right panel.

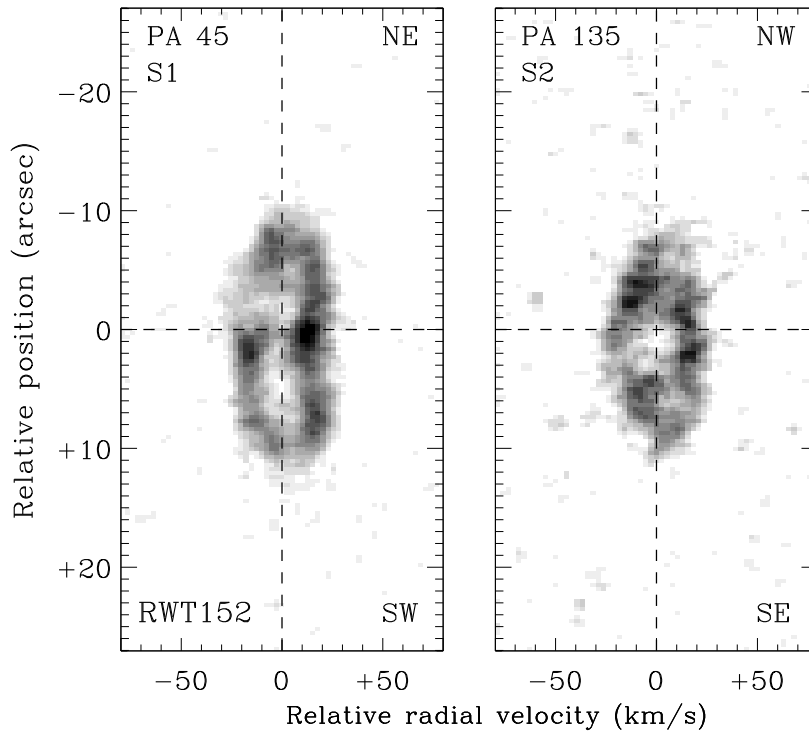


Figure 12. Grey-scale, PV maps derived from the high-resolution, long-slit $[O\text{III}]$ spectra of RWT 152. Grey-levels are linear. The continuum of the central star has been removed (using the *background* IRAF task) and its position is marked with a dashed horizontal line. A 3×3 box smooth was used for the representation.

Table 4. Emission line intensities in RWT 152.

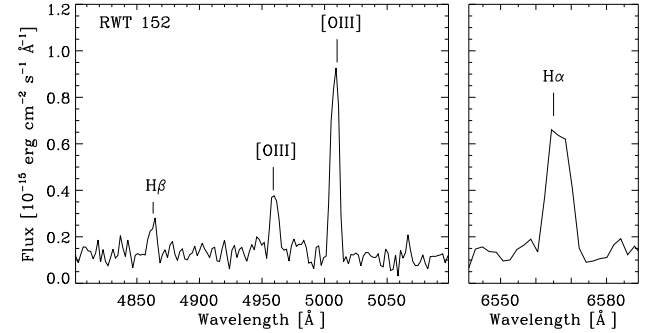
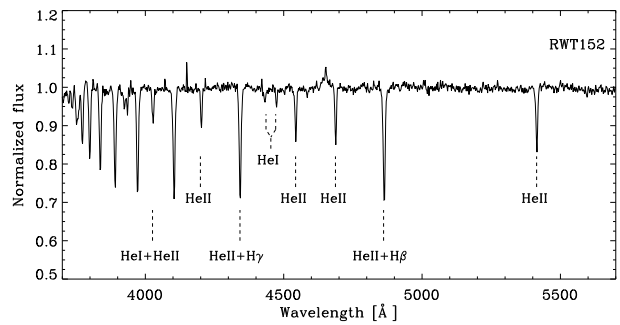
Line	$f(\lambda)$	$I(\lambda) I(\text{H}\beta)=100$
H β λ 4861	0.000	100 ± 3
[O III] λ 4959	-0.023	209 ± 3
[O III] λ 5007	-0.034	591 ± 3
H α λ 6563	-0.323	285 ± 4

$c(\text{H}\beta) = 0.46$
 $\log F_{\text{H}\beta}(\text{erg cm}^{-2} \text{s}^{-1}) = -14.97$

could be suggested that the CSs of Abell 36 and DeHt 2 are also binaries, although, to the best of our knowledge, no direct evidence exists for such binaries. It is interesting to note that both Abell 36 and DeHt 2 contain off-center CSs, which could be considered as an indirect evidence for a binary CS (e.g., Soker et al. 1998). Although it is true that some binary CSs appear off-center, inferring a binary CS from its off-center position only should be seen with caution. Given that DeHt 2 and, perhaps, Abell 36 are evolved PNe, the off-center CSs could be caused by deformation in the shell due to, for instance, interaction with the interstellar medium (Jones et al. 2010; Frew et al. 2014), and/or amplification through evolution of (originally small) asymmetries in the ejection process. In the case of Abell 36, interaction shell-collimated outflows could also contribute to create asymmetries in the shell. The case of the off-center CS of RWT 152 looks different because of the more symmetric shell. However, RWT 152 may be a very distant PN and a higher spatial resolution is necessary to investigate possible asymmetries in the shell, which are already suggested by the distortions in the kinematics. In any case, these three PNe are good candidates to host binary CSs (see also below), and dedicated observations of their CSs should be obtained to search for possible companions.

The nebular spectra of Abell 36 indicates high excitation, as shown by the presence of [Ar IV] and strong He II λ 4686 emission lines. The nebular spectra of DeHt 2 and RWT 152 also indicate high excitation but no emission lines from heavy elements (except [O III]) are detected. If other emission lines exist in these two PNe, they should be very faint. The CSs of Abell 36 and DeHt 2 present very similar atmospheric parameters (Table 1). Therefore, similar emission lines could be expected, unless the physical conditions and/or chemical abundances are very different in both PNe. The CS of RWT 152 has a relatively low T_{eff} and, in principle, low-excitation emission lines should be present in the nebula. The nebular spectra of DeHt 2 and RWT 152 are very similar to that of PN G 075.9+11.6 (Aller et al. 2013), in which only [O III] and Balmer emission lines have been detected. Following these authors, a probable explanation for the peculiar nebular spectra of DeHt 2 and RWT 152 is a deficiency in heavy elements in the nebula. Such a deficiency may be expected in PNe that originate from low-mass progenitors (see, e.g., IC 2149, Vázquez et al. 2002) and it would be consistent with the idea that sdOs evolve from low-mass progenitors (see, e.g., Heber 2009). Deep spectroscopy of these PNe is crucial to detect faint emission lines and to obtain their chemical abundances.

It is interesting to compare the properties of PN+sdO systems. A search in the literature suggests 33 PNe with sdO CS, although in several cases this classification is doubtful or not confirmed (see Weidman & Gamen 2011). For instance, the CS of NGC 2371 is classified as sdO in SIMBAD but as WR-PG 1159 by Herald & Bianchi (2004); the CS of NGC 6026 is classified as WD/sdO by de Marco (2009), as a pre-WD/WD by Hillwig et al. (2010) but as


Figure 13. Nebular spectrum of RWT 152 obtained by integrating the detected emission lines 4.3 and 8.6 arcsec northern of RWT 2 along PA = 0°.

Figure 14. Normalized optical spectrum of the central star of RWT 152. Some of the absorption lines (specially He I and He II) are marked.

OB by Weidman & Gamen (2011); in the case of NGC 1514, the hot star in its binary CS has been classified as sdO (Kohoutek 1967) but a recent spectral analysis (Aller et al. 2014, in preparation) does not allow us to establish a firm classification. If we restrict to those objects with a more confident classification, the number of PN+sdO systems is 18. Table 5 lists these PNe (columns 1 and 2), their morphology and some comments about nebular structures present in them (column 3), the binary nature of the CSs (column 4), and the corresponding references (column 5). We emphasize that the discussion below does not critically depends on whether some of the possible PN+sdO systems are added to the list and/or whether some of the objects in Table 5 are removed. We note that our Table 5 shares several objects with Table 1 by Miszalski et al. (2009). These authors analyze the morphology of PNe with close binary CSs while we focus in the morphology and presence of binaries in sdO CSs.

An inspection of the properties of PN+sdO systems reveals that most of these PNe are very faint, suggesting that they are in a moderately or very evolved stage. A noticeable exception is the Stingray nebula (Hen 3-1357), a very young PN (Parthasarathy et al. 1995) whose CS (SAO 244567) has recently been identified as an sdO (Reindl et al. 2014). If we attend to the morphology, the sample is dominated by elliptical and bipolar shapes with only an object (DS 2) presenting a round morphology. Moreover, many of these PNe show multiple structures, jet-like outflows or point-symmetric structures that could be related to the action of bipolar collimated outflows. It is also remarkable that many PN+sdO systems host binary CSs, suggesting that binary CSs may play an important role in the formation of PN+sdO systems. Finally, a large

Table 5. Properties PN+sdO systems

PN G	Name	Morphology / Comments	Binary CS	References
009.6+10.5	Abell 41	Bipolar	Y	(1), (2), (3)
009.8–07.5	GJJC 1	Irregular / Cometary-like	?	(4),(5)
027.6+16.9	DeHt 2	Elliptical / Spheroidal shell and bipolar outflows at different orientations	?	(6)
053.8–03.0	Abell 63	Bipolar / Jets	Y	(7),(8),(9), (10)
055.4+16.0	Abell 46	Elliptical-Bipolar	Y	(9),(11),(12),(13)
065.0–27.3	K 648	Elliptical / Two elliptical shells and halo	?	(14)
075.9+11.6	2M1931+4324	Multishell / Bipolar and elliptical shell at different orientations	Y	(15),(16)
136.3+05.5	HFG 1	Irregular	Y	(17),(18)
215.6+03.6	NGC 2346	Bipolar	Y	(9),(12),(19)
219.2+07.5	RWT 152	Bipolar	?	(6),(20)
272.1+12.3	NGC 3132	Elliptical	Y	(21),(22)
273.6+06.1	LSS 1362	Irregular-Elliptical	N	(23),(24)
279.6–03.1	He 2-36	Elliptical / Point-symmetry	?	(25),(26)
283.9+09.7	LSS 2018 (DS 1)	Bipolar-Irregular / Low-ionization structures	Y	(9),(27)
318.4+41.4	Abell 36	Elliptical / Inner and (point-symmetric) outer spheroids at different orientations	?	(6),(20)
331.3–12.1	Hen 3–1357	Multishell / Bipolar and elliptical shells and jets	?	(28),(29)
335.5+12.4	LSE 125 (DS 2)	Round	N	(27),(30)
339.9+88.4	LoTr 5	Bipolar	Y	(31),(32)

(1) Bruch et al. (2001); (2) Shimanskii et al. (2008); (3) Jones et al. (2010) (4) Borkowsky et al. (1993); (5) Rauch et al. (1998); (6) This work; (7) Pollacco & Bell (1997); (8) Tsessevich (1977); (9) Miszalski et al. (2009); (10) Mitchell et al. (2007); (11) Stanghellini et al. (2002); (12) Bond & Livio (1990); (13) Ritter & Kolb (2003); (14) Alves et al. (2000); (15) Aller et al. (2013); (16) Jacoby et al. (2012); (17) Heckathorn et al. (1982); (18) Grauer et al. (1987); (19) Kohoutek & Senkbeil (1973); (20) Østensen (2006); (21) Ciardullo et al. (1999); (22) Monteiro et al. (2000); (23) Chu et al. (2009); (24) Heber et al. (1988); (25) Corradi & Schwarz (1993); (26) Méndez (1978); (27) Drilling (1983); (28) Bobrowsky et al. (1998); (29) Reindl et al. (2014); (30) Hua et al. (1998); (31) van Winckel et al. (2014); (32) Graham et al. (2004)

fraction of these systems are observed at a relatively high Galactic latitude. In particular, 11 PNe in Table 1 have $|b| > 10^\circ$ and 15 have $|b| > 7^\circ$. Although the number of objects is small to drawn firm conclusions, the relatively high Galactic latitudes are more typical of round PNe evolving from low-mass progenitors (Corradi & Schwarz 1995; Stanghellini et al. 2002). Remarkably, low-mass progenitors are generally expected for sdOs (see above) and, in addition, sdOs are normally located at high Galactic latitudes. However, one would not expect a large fraction of complex PNe resulting from low-mass progenitors. These results and the large fraction of binary CSs in PN+sdO systems point out that the key parameter to form a complex PN is a binary CS rather than the mass of the progenitor. This conclusion is reinforced by recent results by, e.g., Miszalski et al. (2009), Boffin et al. (2012), Corradi et al. (2014), and Jones et al. (2014) who found that most PNe with close binary CS present complex morphologies.

sdOs associated to PNe represent a very small fraction of the ≥ 800 known sdOs (Østensen 2006). This number could increase as more CSs may be classified as sdO (e.g., Reindl et al. 2014). In this respect, we note the lack of firm classifications for many CS of PNe, which are crucial to identify new sdO among CSs. On the other hand, a recent image survey of ≈ 80 “classical” sdOs (Aller et al., in preparation) to search for associated PNe has identified only a new case (Aller et al. 2013). Nevertheless, given the intrinsic faintness of these PNe, much deeper surveys should be carried out to identify more cases. Several evolutionary paths are considered for the formation of sdOs (see Heber 2009) and, in the case of PN+sdO systems, evolution through asymptotic giant branch (AGB) and post-AGB phases appears to be the most suitable one. For the rest of sdOs (those without a PN), other evolutionary paths (post-red giant branch, post-extended horizontal branch evolution, or star mergers) should be considered (Alves et al. 2000; Napiwotzki 2008; Heber 2009). Nevertheless, if sdO evolution proceeds very slowly, the AGB/post-AGB evolution of a fraction of sdOs

may go unnoticed if the nebula has dispersed before being photoionized. In any case, identification of new PN+sdO systems, and detailed studies of the known ones are important because these systems may provide clues about the formation of complex PNe and sdO evolution.

5 CONCLUSIONS

We have presented and analyzed narrow-band direct images, and high- and low-resolution, long-slit spectra of Abell 36, DeHt 2, and RWT 152, three PNe for which detailed spatio-kinematical analysis had not been carried out before. This analysis has been complemented with low-resolution, long-slit spectra that have allowed us to describe the spectral characteristics of the nebula and their CSs. The main conclusions of this work can be summarized as follows.

Abell 36 presents a point-symmetric elliptical morphology but the spatio-kinematical analysis reveals that it consists of a spheroidal shell and two bright point-symmetric arcs, attributable to bipolar, rotating outflows; the collimated outflows seems to have bored parts of the spheroid. DeHt 2 appears as an elliptical PN in direct images but our analysis strongly suggests that it has formed through two different ejection events, with the last one being more collimated than a previous ellipsoidal shell; evidence also exists in DeHt 2 for collimated outflow-shell interaction. RWT 152 is a bipolar PN with an equatorial ring. The complex structures of Abell 36 and DeHt 2 suggest that binary central stars may be involved in their formation.

The nebular spectra of the three PNe indicate a high excitation but only Abell 36 exhibits emission lines different from those due to Balmer, [O III], and He II. In DeHt 2 and RWT 152 the nebular spectra suggest a possible deficiency in heavy elements.

The spectra of the three CSs present narrow absorption lines, being the He II $\lambda 4686$ absorption particularly prominent. These characteristics, and the published atmospheric parameters strongly

suggest a sdO nature for these CSs. Thus, these sdOs have most probably evolved through AGB and post-AGB phases.

The number of sdOs surrounded by PNe is very scarce (~ 18). This number could be biased by the intrinsic faintness of the associated PNe, and by the lack of a firm classification for many CS of PNe. Very deep images of more sdOs, and analysis of high quality CS spectra are necessary to identify new PN+sdO systems. On the other hand, if sdOs originate from low-mass progenitors, the non-detection of more PN+sdO systems could be, at least for a certain fraction of sdOs, a consequence of the dissipation of the nebula before being photoionized, due to the slow evolution of the CS.

We have compared properties of the more confident PN+sdO systems and found that most of them are relatively or very evolved PNe, present collimated outflows or signs that collimated outflows have been involved in their formation, host binary central stars, and are observed at relatively high Galactic latitudes. These properties and other published results reinforce the idea that the formation of complex PNe is related to binary stars rather than to the progenitor mass. More studies of PN+sdO systems could provide interesting information about formation of complex PNe and sdO evolution.

ACKNOWLEDGMENTS

We thank our anonymous referee for his/her useful comments that have improved the interpretation and discussion of the data. This paper has been supported partially by grant AYA 2011-24052 (AA, ES), AYA 2011-30228-C3-01 (LFM), and AYA 2011-30147-C03-01 (RO) of the Spanish MICINN, and by grant INCITE09312191PR (AA, AU, LFM) of Xunta de Galicia, all of them partially funded by FEDER funds. Partial support by grant 12VI20 of the Universidad de Vigo is also acknowledged. LO acknowledges support by project PROMEP/103.5/12/3590. RV acknowledges support from UNAM-DGAPA-PAPIIT grant IN107914. Authors also acknowledge the staff at OAN-SPM (in particular to Mr. Gustavo Melgoza-Kennedy), Calar Alto, and Roque de los Muchachos Observatories for support during observations. We acknowledge support from the Faculty of the European Space Astronomy Centre (ESAC). This research has made use of the SIMBAD database, operated at the CDS, Strasbourg (France), Aladin, NASA's Astrophysics Data System Bibliographic Services, and the Spanish Virtual Observatory supported from the Spanish MEC through grant AYA2008-02156.

REFERENCES

Abell G. O., 1966, *ApJ*, 144, 259
 Acker A., Marcout J., Ochsenein F., Stenholm B., Tylenda R., Schohn C., 1992, *secg.book*,
 Acker A., Fresneau A., Pottasch S. R., Jasniewicz G., 1998, *A&A*, 337, 253
 Aller A., et al., 2013, *A&A*, 552, A25
 Alves D. R., Bond H. E., Livio M., 2000, *AJ*, 120, 2044
 Boffin H. M. J., Miszalski B., Rauch T., Jones D., Corradi R. L. M., Napiwotzki R., Day-Jones A. C., Köppen J., 2012, *Sci*, 338, 773
 Bohuski T. J., Smith M. G., 1974, *ApJ*, 193, 197
 Bond H. E., Livio M., 1990, *ApJ*, 355, 568
 Bobrowsky M., Sahu K. C., Parthasarathy M., García-Lario P., 1998, *Natur*, 392, 469

Borkowski K. J., Tsvetanov Z., Harrington J. P., 1993, *ApJ*, 402, L57
 Brocklehurst M., 1971, *MNRAS*, 153, 471
 Bruch A., Vaz L. P. R., Diaz M. P., 2001, *A&A*, 377, 898
 Cahn J. H., Kaler J. B., 1971, *ApJS*, 22, 319
 Cahn J. H., Kaler J. B., Stanghellini L., 1992, *A&AS*, 94, 399
 Chromey F. R., 1980, *AJ*, 85, 853
 Chu Y.-H., et al., 2009, *AJ*, 138, 691
 Ciardullo R., Bond H. E., Sipior M. S., Fullton L. K., Zhang C.-Y., Schaefer K. G., 1999, *AJ*, 118, 488
 Corradi R. L. M., Schwarz H. E., 1993, *A&A*, 273, 247
 Corradi R. L. M., et al., 2014, *MNRAS*, 441, 2799
 Dengel J., Hartl H., Weinberger R., 1980, *A&A*, 85, 356
 De Marco O., 2009, *PASP*, 121, 316
 Drilling J. S., 1983, *ApJ*, 270, L13
 Ebbets D. C., Savage B. D., 1982, *ApJ*, 262, 234
 Frew D. J., Bento J., Bojicic I. S., Parker Q. A., 2014, *arXiv*, arXiv:1403.7847
 Geier S., et al., 2011, *AIPC*, 1331, 163
 Geier S., 2013, *EPJWC*, 43, 4001
 Goldman D. B., Guerrero M. A., Chu Y.-H., Gruendl R. A., 2004, *AJ*, 128, 1711
 Graham M. F., Meaburn J., López J. A., Harman D. J., Holloway A. J., 2004, *MNRAS*, 347, 1370
 Grauer A. D., Bond H. E., Ciardullo R., Fleming T. A., 1987, *BAAS*, 19, 643
 Guerrero M. A., et al., 2008, *ApJ*, 683, 272
 Guerrero M. A., Miranda, L. F., 2012, *A&A*, 593, 47
 Guillén P. F., Vázquez R., Miranda L. F., Zavala S., Contreras M. E., Ayala S., Ortiz-Ambriz A., 2013, *MNRAS*, 432, 2676
 Heber U., Werner K., Drilling J. S., 1988, *A&A*, 194, 223
 Heber U., 2009, *ARA&A*, 47, 211
 Heckathorn J. N., Fesen R. A., Gull T. R., 1982, *A&A*, 114, 414
 Herald J. E., Bianchi L., 2004, *ApJ*, 609, 378
 Herrero A., Manchado A., Mendez R. H., 1990, *Ap&SS*, 169, 183
 Hillwig T. C., Bond H. E., Afşar M., De Marco O., 2010, *AJ*, 140, 319
 Hua C. T., Dopita M. A., Martinis J., 1998, *A&AS*, 133, 361
 Hua C. T., Kwok S., 1999, *A&AS*, 138, 275
 Jacoby G., De Marco O., Howell S., Kronberger M., 2012, *AAS*, 219, #418.02
 Jones D., et al., 2010, *MNRAS*, 408, 2312
 Jones D., Boffin H. M. J., Miszalski B., Wesson R., Corradi R. L. M., Tyndall A. A., 2014, *A&A*, 562, A89
 Kilkenny D., O'Donoghue D., Koen C., Stobie R. S., Chen A., 1997, *MNRAS*, 287, 867
 Kohoutek L., Hekela J., 1967, *BAICz*, 18, 203
 Kohoutek L., Senkbeil G., 1973, *MSRSL*, 5, 485
 Latour M., Fontaine G., Chayer P., Brassard P., 2013, *ApJ*, 773, 84
 Leone F., Martínez González M. J., Corradi R. L. M., Privitera G., Manso Sainz R., 2011, *ApJ*, 731, L33
 Manchado A., Guerrero M. A., Stanghellini L., Serra-Ricart M., 1996, *iacm.book*,
 Meaburn J., López J. A., Gutiérrez L., Quiróz F., Murillo J. M., Valdéz J., Pedrayez M., 2003, *RMxAA*, 39, 185
 Méndez R. H., 1978, *MNRAS*, 185, 647
 Méndez R. H., Gathier R., Simon K. P., Kwitter K. B., 1988, *A&A*, 198, 287
 Méndez R. H., 1991, *IAUS*, 145, 375
 Miranda L. F., Solf J., 1992, *A&A*, 260, 397

- Miszalski B., Acker A., Parker Q. A., Moffat A. F. J., 2009, *A&A*, 505, 249
- Mitchell D. L., Pollacco D., O'Brien T. J., Bryce M., López J. A., Meaburn J., Vaytet N. M. H., 2007, *MNRAS*, 374, 1404
- Monteiro H., Morisset C., Gruenwald R., Viegas S. M., 2000, *ApJ*, 537, 853
- Montez R., Jr., De Marco O., Kastner J. H., Chu Y.-H., 2010, *ApJ*, 721, 1820
- Nakanishi H., Sofue Y., 2003, *PASJ*, 55, 191
- Napiwotzki R., 1999, *A&A*, 350, 101
- Napiwotzki R., 2001, *A&A*, 367, 973
- Napiwotzki R., 2008, *ASPC*, 392, 139
- Napiwotzki R., Schoenberner D., 1995, *A&A*, 301, 545
- Østensen R. H., 2006, *BaltA*, 15, 85
- Parthasarathy M., et al., 1995, *A&A*, 300, L25
- Phillips J. P., 2005, *MNRAS*, 357, 619
- Pollacco D. L., Bell S. A., 1997, *MNRAS*, 284, 32
- Pritchett C., 1984, *A&A*, 139, 230
- Ramos-Larios G., Guerrero M. A., Vázquez R., Phillips J. P., 2012, *MNRAS*, 420, 1977
- Rauch T., Dreizler S., Wolff B., 1998, *A&A*, 338, 651
- Reindl N., Rauch T., Parthasarathy M., Werner K., Kruk J. W., Hamann W.-R., Sander A., Todt H., 2014, *A&A*, 565, A40
- Ritter H., Kolb U., 2003, *A&A*, 404, 301
- Seaton M. J., 1979, *MNRAS*, 187, 73P
- Shimanskii V. V., Borisov N. V., Sakhibullin N. A., Sheveleva D. V., 2008, *ARep*, 52, 479
- Soker N., Rappaport S., Harpaz A., 1998, *ApJ*, 496, 842
- Stanghellini L., Villaver E., Machado A., Guerrero M. A., 2002, *ApJ*, 576, 285
- Tocknell J., De Marco O., Wardle M., 2014, *MNRAS*, 439, 2014
- Traulsen I., Hoffmann A. I. D., Rauch T., Werner K., Dreizler S., Kruk J. W., 2005, *ASPC*, 334, 325
- Tsessevich V. P., 1977, *IBVS*, 1320, 1
- Van Winckel H., Jorissen A., Exter K., Raskin G., Prins S., Perez Padilla J., Merges F., Pessemier W., 2014, *A&A*, 563, L10
- Vázquez R., Miranda L. F., Torrelles J. M., Olguín L., Benítez G., Rodríguez L. F., López J. A., 2002, *ApJ*, 576, 860
- Vázquez R., Miranda L. F., Olguín L., Ayala S., Torrelles J. M., Contreras M. E., Guillén P. F., 2008, *A&A*, 481, 107
- Wareing C. J., Zijlstra A. A., O'Brien T. J., 2007, *MNRAS*, 382, 1233
- Weidmann W. A., Gamen R., 2011, *A&A*, 526, A6
- Włodarczyk K., Olszewski P., 1994, *AcA*, 44, 407